

Metal Grid Structures for Enhancing the Stability and Performance of Solution-Processed Organic Light-Emitting Diodes

Gregory Burwell,* Nicholas Burridge, Oskar J. Sandberg, Eloise Bond, Wei Li, Paul Meredith, and Ardalan Armin*

Transparent conducting electrodes (TCEs) are key components of optoelectronic devices where input or output light coupling are central functions—for example, solar cells, light-emitting diodes, or displays. Indium tin oxide (ITO) has been the TCE of choice for over three decades, and there are few alternatives. The characteristic size of devices made with ITO is often limited to a few centimeters because of the intrinsic sheet resistance. This is an obstacle for scaling thin film photovoltaics and lighting platforms to technologically-relevant large areas. In this article, the use of metallic micro-grids is investigated to improve sheet resistance–visible transparency balance of TCEs, resulting in improved performance and stability of organic light-emitting diodes (OLEDs). Finite element models are used to simulate OLEDs pixels on ITO with metal grids, and these simulations are supported by experimental performance analysis. The reduced potential drop from the presence of grids is shown to lower the Joule heating at the TCE resulting in higher power conversion efficiency and luminosity, as well as improved device stability. Such a strategy could be a very effective way of not only reducing indium usage but also opening new higher resistance TCEs to technological viability.

color quality, and wide viewing angles from emissive OLED displays have facilitated their commercial success.^[2,3] Solution-processed and low-temperature evaporated OLEDs are amenable to high-volume production methods that are compatible with thin, conformal, and flexible substrates, such as roll-to-roll processing or printing.^[4] As issues related to scaling pixel sizes are addressed,^[5] OLEDs could become a technology choice for diffuse, low luminance, large area lighting panels that are thin and lightweight.^[6] As increasingly efficient OLED materials are developed and their production is scaled using methods with low embodied energy, OLED lighting panels may help to reduce worldwide energy consumption for lighting using sustainable materials.^[7]

Despite the great success of OLEDs in the display technology market, for lighting applications OLEDs have not to date been widely adopted. Several factors have played a role in this regard, a central one being the requirement for relatively high electrical drive currents in large area OLEDs limited by the relatively high sheet resistance ($\approx 10\text{--}20 \Omega \square^{-1}$) of the transparent conductive electrodes (TCEs). Additionally, for large-area printed OLEDs intended for lighting applications, standard “lab-scale” deposition methods such as spin-coating are not appropriate, and one must turn instead to printing methodologies. Furthermore, since point defect densities scale exponentially with area in thin solution-processed layers (typically efficient OLEDs have emissive layer thicknesses of ≈ 100 nm), high production yields over large areas naturally require much thicker devices with non-optimal performance characteristics.^[8]


Minimizing defects also requires a low surface roughness (indeed flat) deposition substrate, and this is where the quality of the TCE also plays a role since in a conventional architecture it is the support electrode. The required electrical and optical properties of TCEs impose additional constraints on the choice of available materials. In practical terms average visible transmittances $>80\%$ (with flat spectral responses) and resistivities $<10^{-3} \Omega \cdot \text{cm}$ are required.^[7,9,10] For state-of-the-art metal oxide TCEs such as indium tin oxide (ITO) this means a sheet resistance of order $10\text{--}20 \Omega \square^{-1}$ —very much on the borderline of

1. Introduction

Organic light-emitting diodes (OLEDs) are a rapidly evolving technology for displays and lighting panels.^[1] Properties such as low drive powers for high brightness, enhanced

Dr. G. Burwell, N. Burridge, Dr. O. J. Sandberg, Dr. W. Li, Dr. A. Armin, Prof. P. Meredith
Department of Physics
Singleton Campus
Swansea University
Swansea SA2 8PP, UK
E-mail: g.burwell@swansea.ac.uk; Ardalan.armin@swansea.ac.uk

E. Bond
SPTS Technologies Ltd
Ringland Way, Newport NP18 2TA, UK

 The ORCID identification number(s) for the author(s) of this article can be found under <https://doi.org/10.1002/aelm.202000732>.

© 2020 The Authors. Advanced Electronic Materials published by Wiley-VCH GmbH. This is an open access article under the terms of the Creative Commons Attribution-NonCommercial License, which permits use, distribution and reproduction in any medium, provided the original work is properly cited and is not used for commercial purposes.

DOI: 10.1002/aelm.202000732

what is achievable given the required trade-off between free carrier density and optical absorption. Yet, although materials such as carbon nanotube mats, thin graphene layers, conductive polymers, and metallic nanowires have shown some promise as TCEs,^[11–14] it is relatively thin, evaporated metal oxide layers (ITO, Aluminum-doped-Zinc Oxide and Fluorine-doped-Tin Oxide) that dominate the technological landscape including for OLEDs.^[9] Other advances, including the use of poly(3,4-ethylenedioxythiophene) polystyrene sulfonate PEDOT:PSS grid lines,^[15] and the use of transparent conductive films made from solution-processable transparent conductive materials have been demonstrated in recent years, which indicate a route to low-cost fully printed optoelectronic devices.^[16–19]

Owing to their small pixel size, the series resistance of the TCE for each pixel in an OLED display does not pose a substantial issue. However, above active area sizes of $\approx 1 \text{ cm}^2$, even the best TCEs become a performance-limiting consideration. The increasingly large TCE series resistance as a function of device area not only causes power loss, but also undesirable Joule heating which can rapidly deteriorate luminance uniformity, and device lifetimes.^[20,21] Consequently, currently available monolithic TCE materials (with sheet resistances $\approx 10 \Omega \square^{-1}$) are not suitable for the production of competitive large-scale OLED lighting panels.^[22] A proposed solution to this problem is the combinatorial use of metallic grids with transparent conductive oxides. These have been demonstrated to improve the performance of large-area OLEDs,^[23] and are also potentially useful for other solution-processable optoelectronic applications, such as photovoltaics.^[8] Applied on top of a TCE material such as ITO, metal grids can reduce the effective sheet resistance (R_{sheet}), of the TCE, and their positive impact on large-area OLED thermal and optical properties has been demonstrated, largely for lighting applications.^[23]

Motivated by these observations, in this current work, finite element modeling (FEM) was used to compare typical OLED devices with ITO TCEs (“ITO-OLEDs”), and equivalent devices with metal grids added to the TCE (“MG-OLEDs”). The heat generated in the TCE by Joule heating was compared and estimates of operational temperatures for different pixel types obtained. Geometrically optimized metal grid structures were fabricated on ITO/glass substrates using standard lithographic techniques. Solution-processable conjugated polymer Super Yellow (a poly[2-methoxy-5-(2'-ethylhexyloxy)-1,4-phenylene vinylene] (MEH-PPV) copolymer) OLED devices were fabricated on ITO substrates with metal grid structures, and these MG-OLEDs compared operationally to ITO-OLED devices. Simulation and experimental results of layers deposited at different thicknesses were also compared to investigate the contribution that sheet resistance of the TCE and the thickness of the active layer play in defining OLED figures of merit, and thus, predictive structure-property relationships have been derived.

2. Results and Discussion

2.1. Electrical Simulations of OLED Devices

Finite element modeling was utilized to simulate the electrical properties of large-area devices with different micro-grid geometries. A schematic of the simulated OLEDs on

unmodified ITO (ITO-OLEDs) and ITO with metal grid structures (MG-OLEDs) is shown in **Figure 1a**. A 2D:1D:2D model (TCE anode: emissive layer: metal cathode) was used to simulate the behavior of a large-area device for a given small-area current density-voltage (JV) profile. A simulated JV profile of a 130 nm thick MEH-PPV type emissive layer was selected as an example emissive layer, the details of which are outlined in the following section.

To demonstrate the effect of pixel size, JV characteristics were simulated for $5 \text{ cm} \times 5 \text{ cm}$ and $1 \text{ cm} \times 1 \text{ cm}$ OLED pixels (**Figure 1b**). With $5 \text{ cm} \times 5 \text{ cm}$ pixel area, the resistive losses are considerably greater in ITO-OLEDs. This leads to a steeper gradient in the large-area JV curves of MG-OLEDs (blue triangles) in the forward bias region compared to ITO-OLEDs (green triangles). In comparison, the $1 \text{ cm} \times 1 \text{ cm}$ pixels have a smaller difference in slope between the MG-OLED (black squares) and the ITO-OLED (red circles), attributed to lower resistive losses. As $\approx 1 \text{ cm}^2$ pixels are more representative of devices investigated at research scales, the work that follows will focus on this pixel size.

Further understanding of the operation of the metallic grids can be derived from examination of the contour plots from ITO-OLEDs (**Figure 1, left panels**) and MG-OLEDs (**right panels**) which summarize their operation at an average current density of 0.5 A cm^{-2} (applied at the bus-barred edges of the devices). The surface potential of the TCE of the ITO-OLED (**Figure 1c**) has a greater voltage drop at the center of the device ($\approx 600 \text{ mV}$) compared to that of the MG-OLED ($\approx 30 \text{ mV}$, **Figure 1d**). The presence of the metal grids in the MG-OLEDs provides a surface of equal potential, similar in principle to the bus bars used in silicon photovoltaics.^[24]

The local current density $j_{\perp}(x,y)$ passing through a component of the emissive layer at position (x,y) is calculated from the potential difference across the top and bottom electrodes at a given point from a given small area JV curve [$\hat{j}(V)$]:

$$j_{\perp}(x,y) = \hat{j}[V(x,y)]: V(x,y) = \psi^{\text{te}}(x,y) - \psi^{\text{be}}(x,y) \quad (1)$$

where ψ^{te} and ψ^{be} are the potential of the top electrode, and potential at the bottom electrode, respectively. The variation of surface potential across the TCE, therefore, causes a variation in current density across the device. The current density is maximum at the edges and drops to $\approx 15\%$ at the center of the ITO-OLED (**Figure 1e**), whereas the MG-OLED (**Figure 1f**) varies $< 1.5\%$. This would correspond to an equivalent drop in luminance across the surface of the pixel and would be more pronounced for larger pixel sizes. Equivalent data for $5 \text{ cm} \times 5 \text{ cm}$ pixels are displayed in **Figure S1**, Supporting Information.

As the edges of the device are held at a fixed potential, the potential gradient across the TCE can be expressed as an electric field, $\vec{E}_{\text{appl}} = -\nabla\psi$. The potential gradient across the TCE has a corresponding in-plane current, termed the flux current. From Ohm's law, this flux (parallel) current can be expressed as:

$$j_{\parallel} = \sigma_{\text{TCE}} \vec{E}_{\text{appl}} = -\sigma_{\text{TCE}} \nabla\psi = -\frac{\nabla\psi}{R_{\text{TCE}}} \quad (2)$$

Assuming $\sigma_x = \sigma_y = \sigma_{\text{TCE}}$, that is, the conductance of the TCE is isotropic in the plane, and its inverse is given by

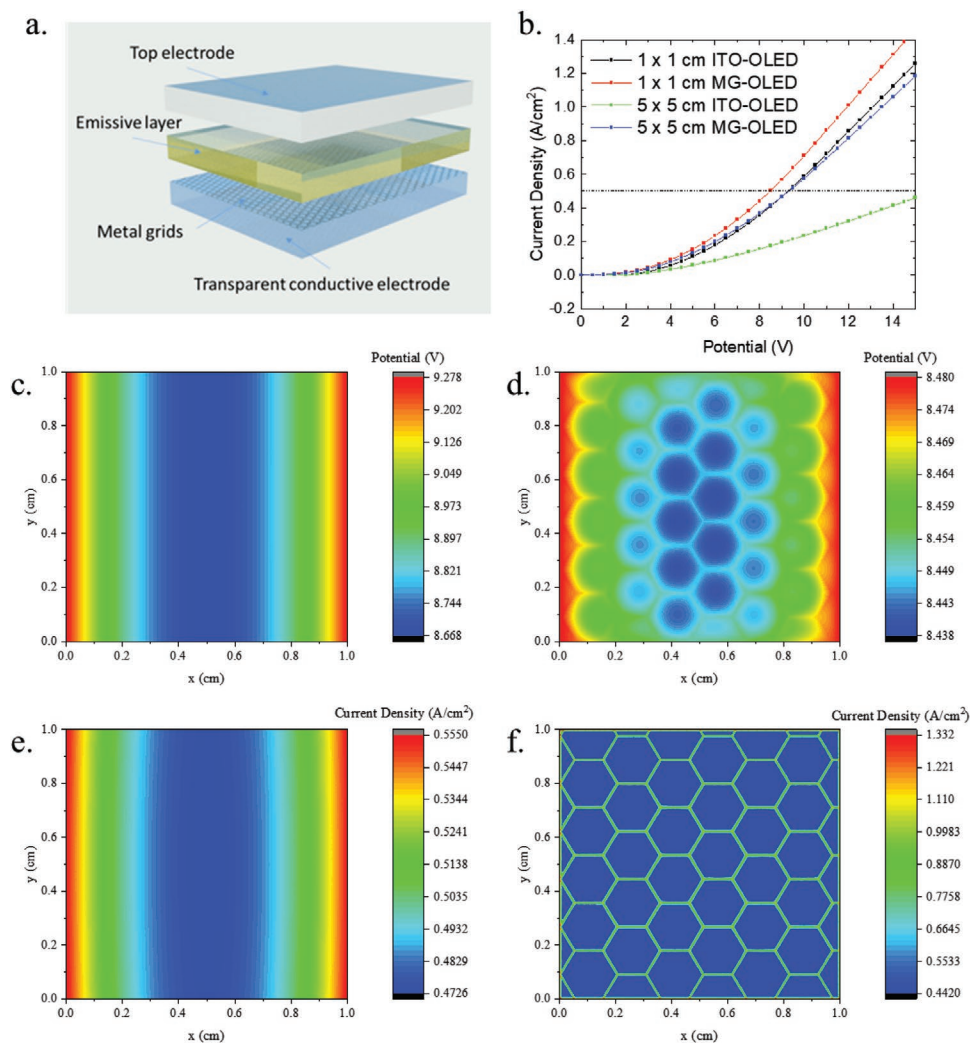


Figure 1. Electrical simulation results from OLED devices a.) Schematic view of the 2D+1D +2D model used in the simulations, consisting of a 2D transparent electrode (with or without metal grids), a thin emissive layer, and a 2D metal electrode b.) Simulated device J/V curves of ITO- and MG-OLEDs generated from the small-area J/V of a 130 nm thick OLED device (see Figure 3a) for 5 cm × 5 cm pixels and 1 cm × 1 cm pixels. Surface potential of the TCE at an applied voltage that corresponds to an average current density of 0.5 A cm⁻², indicated in (b) for c.) ITO-OLED and d.) MG-OLEDs, the resulting current density through the emissive layer for e.) ITO-OLED and f.) MG-OLED.

the sheet resistance, R_{TCE} (in units of $\Omega\text{m m}^{-1} = \Omega \square^{-1}$). As the potential gradient is steeper for the ITO-OLED, the corresponding magnitude of flux current is greater in the ITO regions (Figure 2a), in comparison to that of the MG-OLED (Figure 2b), in which the flux current is concentrated in the metal grid regions but negligible in the ITO regions. This in-plane flux current is distinguished from the out-of-plane current passing between the electrodes through the emissive layer. Whereas a proportion of the latter corresponds to the emissive behavior of the OLED, the in-plane current of the TCE is dissipated as heat.

The heat dissipation (in W cm^{-2}) resulting from the flux current (Ohmic heating) is given by:

$$R_{\text{TCE}} |j_{\parallel}|^2 = \frac{|\nabla\psi|^2}{R_{\text{TCE}}} \quad (3)$$

In the ITO-OLED, the heat dissipation is concentrated at the edges of the pixel (Figure 2c) and confined to the metal grids regions for the MG-OLED (Figure 2d). The overall dissipation is considerably larger in the ITO-OLED (≈ 207 mW) compared to the MG-OLED (≈ 15 mW).

The design of the grid structures in an MG-OLED is a consideration for its optoelectronic properties. It is useful to define the geometric fill factor (GFF), the area of the pixel that is unshadowed by metallic grids. There is a compromise between the electrical performance of the TCE, which is enhanced by large grid areas (low GFF), and the light emitted from the unshadowed regions (high GFF). Varying the width of the grids with fixed pitch had a small but measurable effect on the uniformity and is summarized in Figure S2a, Supporting Information. As the track width of the metal grids is widened, the resultant potential drop is slightly lower, corresponding to a lower overall sheet

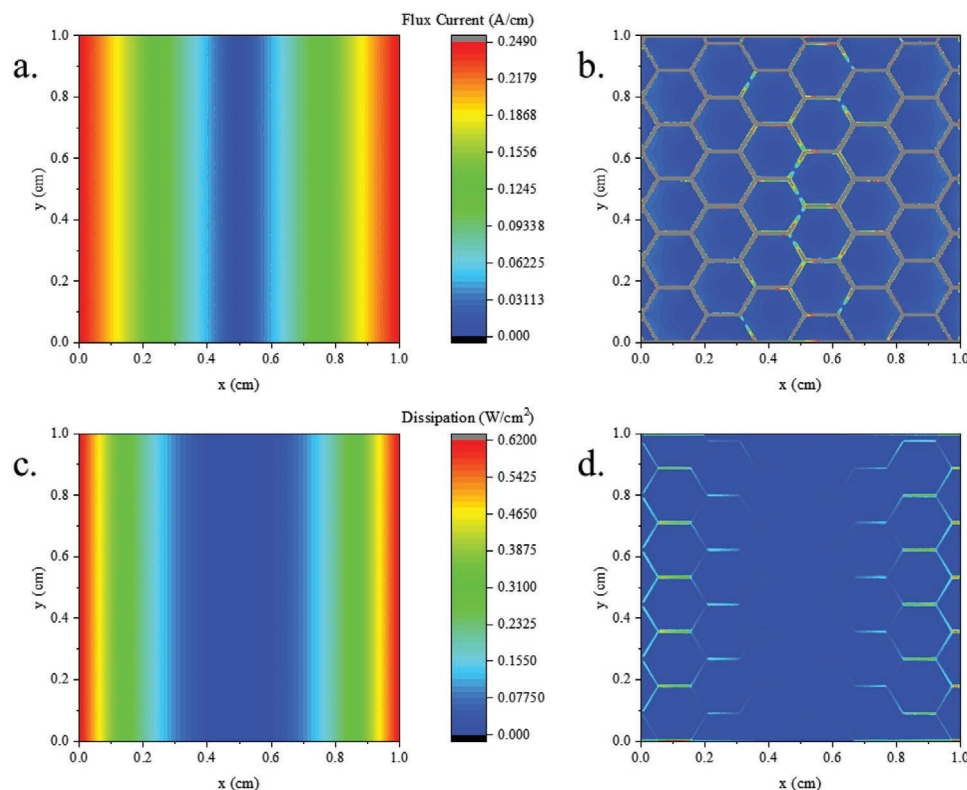


Figure 2. Electrical simulation results from 1 cm² OLED pixels with 0.5 A applied to the edges of the devices. The voltage applied corresponded to an average current density of 0.5 A cm⁻², indicated in Figure 1b. The flux (in-plane) current per unit length for a.) ITO-OLED and b.) MG-OLED. Dissipated power density for c.) ITO-OLED d.) MG-OLED.

resistance, and thus a steeper JV profile. The wider grids will also shadow more of the light from being emitted from the MG-OLED device.

The choice of metal grid geometry also has an impact on the performance of an MG-OLED device. For a given GFF, the use of hexagonal structures was seen to be preferable to other geometries, such as rectangular grids. An example of this is shown in Figure S2b, Supporting Information, which compares rectangular and hexagonally patterned MG-OLED structures with the same GFF. The difference is more pronounced at high GFF (large area unshadowed), indicating that hexagonal geometries are more efficient at providing an equipotential surface.

2.2. Emissive Layer Thickness Dependence and Heat Generation

In the previous section, typical OLED JV characteristics for a 130 nm thick MEH-PPV type emissive layer were used to investigate the effect of adding metallic grids to a TCE such as ITO. As OLED devices may be created with varying active layer thicknesses for different practical purposes (such as reducing defect density, scalability, electro-optical engineering), the small-area JV characteristics of OLEDs can be simulated to understand some of this behavior.

To capture the thickness-dependent behavior at the operating voltages of interest, a 1D device model based on drift-diffusion was used.^[25] At voltages greater than the built-in voltage V_{bi} ,

when the OLED devices are operating in the space-charge-limited current (SCLC) regime, the current density can be approximated by a modified Mott-Gurney law, which gives a d^{-3} dependence of the emissive layer thickness:

$$J_{SCLC} = \frac{9}{8} \zeta \epsilon \epsilon_0 [\mu_n + \mu_p] \frac{(V - V_{bi})^2}{d^3} \quad (4)$$

Here, V is the voltage across the small-area diode, μ_n, μ_p are the (field-dependent) mobilities of electrons and holes, respectively, and ϵ the relative permittivity of the emissive layer, while ϵ_0 is the vacuum permittivity. The prefactor ζ is an enhancement factor accounting for the partial charge neutralization of electrons and holes inside the emissive layer (related to the non-Langevin reduction factor in the area of organic PV), in accordance with the work by Parmenter and Ruppel.^[26–28] At voltages lower than V_{bi} , the diode is strongly limited by diffusion, acting as an internal resistance that increases exponentially with decreasing V ; the resulting current density in this regime follows an exponential voltage dependence.^[29]

This model was used to generate thickness-dependent small-area JV curves of MEH-PPV type OLED materials, as shown in Figure S3a, Supporting Information, of which 130 and 260 nm were selected as representative thick device thicknesses which may be deposited using large-area printing techniques.

Figure 3a shows the small-area JV curves of the emissive layers selected for this comparison. The large-area behavior of 1 cm² ITO- and MG-OLEDs using these materials was then

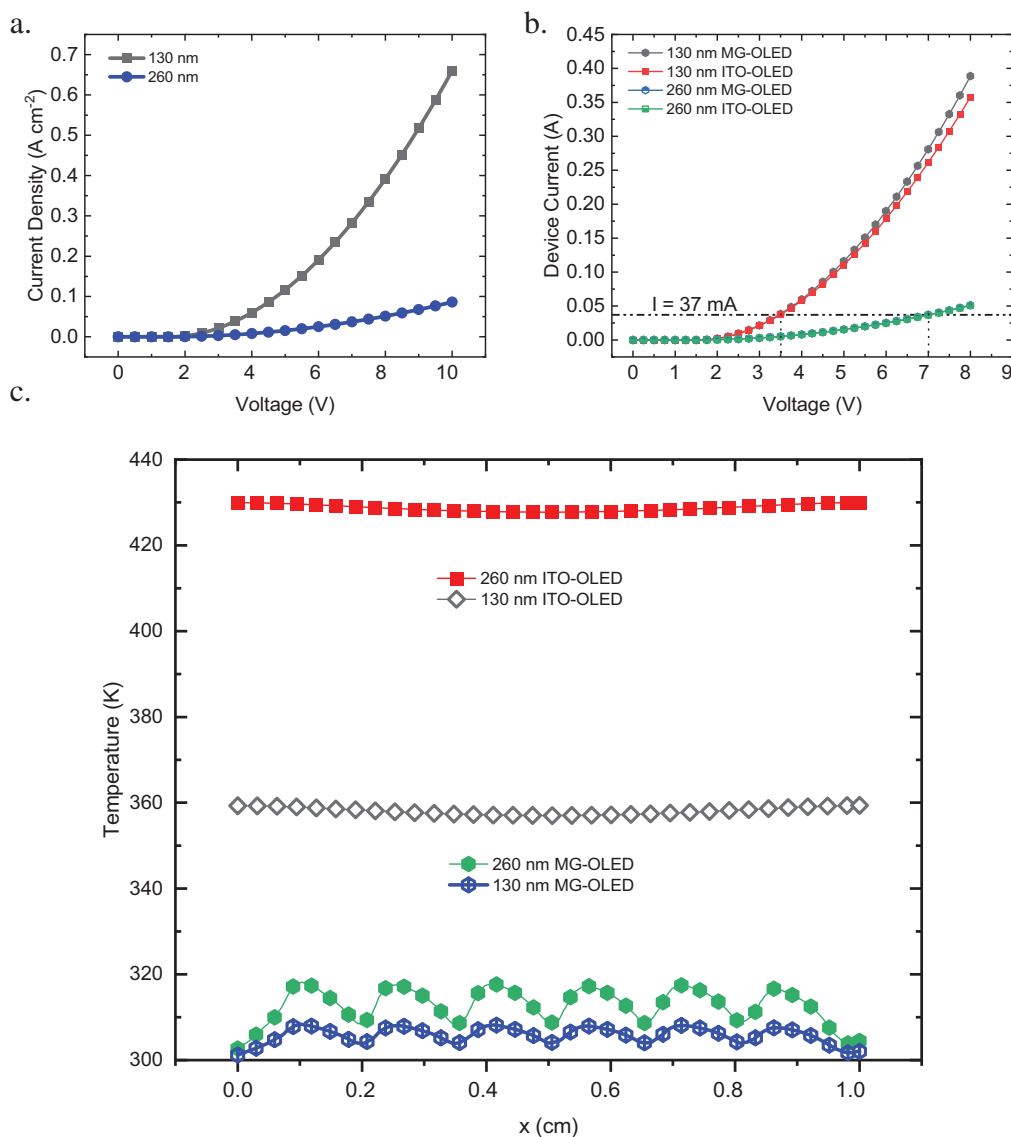


Figure 3. Comparison of heat generation at different layer thicknesses. a.) Simulated small area JV curves for 130 nm thick (black squares) and 260 nm thick (blue circles) for MEH-PPV type OLEDs b.) Comparison of 1 cm^2 130/260 nm ITO/MG-OLEDs. c.) Temperature profiles from heat generation simulations of 130 nm ITO-OLED @37 mA/3.5 V (diamonds) 130 nm MG-OLED @37 mA/3.5 V (blue circles), 260 nm ITO-OLED @37 mA/7.25 V (red squares), 260 nm MG-OLED @37 mA/7.25 V (green circles).

investigated using the FEM methods described in the previous section. The resulting large-area JV curves for these devices are displayed in Figure 3b. Due to the d^{-3} dependence of the small-area JV behavior, the corresponding current at voltages $>V_{bi}$ are much higher for the 130 nm devices. Due to the heat dissipation of the flux current in the TCE (Equation (3)), varying the type of TCE used will affect the operational temperatures of the OLED. Estimates of these operating temperatures were obtained using a heat generation model to compare MG- and ITO-OLEDs. As OLEDs are typically used as current-driven devices, temperatures at comparable currents were investigated.

The resulting temperature profiles across the pixels driven at 37 mA are plotted in Figure 3c. With 130 nm emissive layers, the ITO-OLED (unfilled diamonds) operates at slightly

higher temperatures ($\approx 360 \text{ K}$) than the corresponding MG-OLED (blue circles). Consistent with the heat dissipation model, the temperatures are highest at the edges of the ITO-OLED (where the current is injected). With 260 nm emissive layers, the ITO-OLED (red squares) operates at significantly higher temperatures ($\approx 430 \text{ K}$) than the MG-OLED (green circles). This trend is consistent with the heat dissipation profiles at the TCE for the studied pixels, plotted in Figure S3b, Supporting Information.

As the emissive layer thickness is increased, the heat generated at the TCE in ITO-OLEDs is higher for a given device current. To obtain similar currents, the thicker devices are operated at higher voltages, and the corresponding flux current in the TCE of the ITO-OLED is increased. The use of metal grids

in MG-OLEDs reduces the heat generated at the TCE, and its contribution to the operating temperature of the pixel.

2.3. Exemplification Using Super Yellow OLEDs

Following the simulation work described in the previous section, exemplar OLED structures were fabricated to demonstrate the effect of the metal-grids on the performance of the OLEDs at different thickness regimes. The solution-processable conjugated polymer Super Yellow (SY), which is a poly[2-methoxy-5-(2'-ethylhexyloxy)-1,4-phenylene vinylene] (MEH-PPV) copolymer, was selected as the emissive layer in OLED devices due to its wide availability and well-documented properties in literature.^[30] Super yellow OLEDs were fabricated on unmodified ITO TCEs (ITO-OLEDs), and TCEs with ITO and metal grids (MG-OLEDs) created with microfabrication techniques, reducing the effective sheet resistance of the TCE from $10 \Omega \square^{-1}$ to $<1 \Omega \square^{-1}$ (see Experimental Section). Two thicknesses of Super Yellow MG/ITO OLEDs were studied to investigate the effect of emissive layer thickness, consistent with the thermal simulations in the previous section.

2.4. OLED Performance Enhancement with Metal Grids

External quantum efficiency–electroluminescence (EQE-EL) characterization data of 1 cm^2 ITO-OLED and MG-OLED pixels with $\approx 130 \text{ nm}$ thick Super Yellow layers are summarized in Figure 4. The emission behavior is shown in Figure 4a; the current density (A cm^{-2} , left axis, unfilled points) and luminance (cd m^{-2} , right axis, filled points) follow similar profiles for both ITO- and MG-OLED pixels. Similar to the simulated pixels (Figure 1b), the slope of the JV curve of the MG-OLED is steeper than that of the ITO-OLED. Other resistances not accounted for in the simulated pixels, will also be present in the measured OLED pixels.^[31] Similar trends were also recorded in smaller pixels (Figure S3c, Supporting Information).

The similar profiles of the current density and luminance curves indicate that the proportion of emission to injected current is similar for both ITO- and MG-OLED devices. More

specifically, this can also be seen in the luminous current efficiency curves for ITO-OLED and MG-OLED (Figure S3a, Supporting Information) pixels, given by the ratio of the luminance to current density,^[32] $\eta_{\text{lc}} = \frac{L}{J}$, where L is the luminance (cd m^{-2}) and J is the current density (A m^{-2}), having units of cd A^{-1} . The slight decrease in the current density of the 1 cm^2 MG-OLED at lower voltages may be explained by device fabrication parameters, such as emissive layer uniformity. In contrast, the profiles of current efficiency for 0.15 cm^2 ITO- and MG-OLED pixels overlap (Figure S4d, Supporting Information), indicating that fabrication-related variations are exacerbated at larger pixel sizes.

Luminous efficacy, defined as the ratio of the output luminance to input electrical power, (lm W^{-1}) are plotted for the 1 cm^2 ITO- and MG-OLED pixels against luminance in Figure 4b. It is important to note that it is more illustrative to compare the LE of the pixels against luminance rather than voltage. This is easily demonstrated in the 0.15 cm^2 pixel data, where it is shown that the LE is approximately the same for both pixels plotted against voltage (Figure S4e, Supporting Information), and deviates when plotted against luminance (Figure S4f, Supporting Information). This can be understood using a simple circuit model of a resistor in series with an LED; the series resistor limits the amount of current drawn from the power source, therefore a circuit with a smaller series resistance R_s will consume more power at a given voltage. If the current efficiencies of the LEDs are equivalent, then a corresponding increase in luminance will be measured from the LED, making the overall LE the same at that voltage. At a given luminance, a circuit with a higher R_s requires more input power to compensate for the $I^2 R_s$ losses in the circuit. In contrast to the current efficiency and the EQE, in which the properties related to the emissive layer are the dominant factors, the power (energy) conversion efficiency includes the Ohmic losses at the TCE.

Further evidence of the emissive layer properties not being affected by the reduced sheet resistance can be seen in the similarity of the EQE of both pixels, which are consistently around 2%. In general, the EQE can be expressed as the product of the internal quantum efficiency (IQE) and the light out-coupling efficiency.^[32] The similarity in the EQE curves for

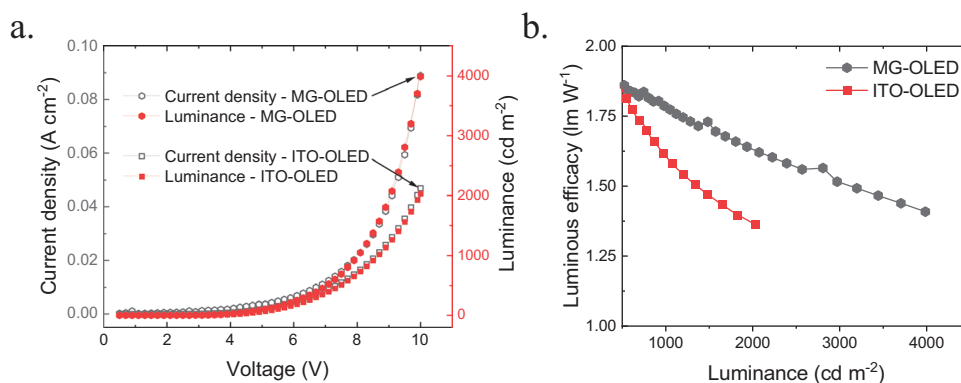


Figure 4. Comparison of 130 nm thick, 1 cm^2 Super Yellow OLED pixels. a.) MG-OLED pixel (hexagons) and a 1 cm^2 ITO-OLED pixel (squares). Luminous flux (red, right axis) and current density (unfilled, left axis) b.) LE plotted against luminance for a MG-OLED pixel (black hexagons), and an ITO-OLED pixel (red squares).

the ITO and MG-OLEDs indicates that neither the IQE nor the outcoupling efficiency are changed significantly by the presence of metal grids in the MG-OLEDs. Overall, significant differences in EQE were not measured between ITO- and MG-OLEDs (Figure S3b, Supporting Information), with the variation in EQE of pixels on each sample being the dominant factor. This is likely due to factors unrelated to the presence of metal grids, such as non-uniformities in the emissive layer thickness or cathode. At 130 nm emissive layer thickness, the dominant difference between Super Yellow MG- and ITO-exemplar OLEDs is understood as a reduced series resistance in the TCE providing higher current densities (and thus higher luminance), and correspondingly higher LE at a given luminance.

2.5. Effect of Joule Heating on Thick OLED Device Stability

Characterization data for ITO-OLED and MG-OLED pixels with ≈ 260 nm thick Super Yellow layers are summarized in Figure 5. In comparison to the thinner emissive layer results, EQE-EL measurements for 260 nm OLED pixels results were, in general, less regular and did not demonstrate a consistent trend between different TCE types from initial measurements. However, device measurements of ITO-OLED pixels were less reproducible, in many instances illumination from the OLEDs ceased during measurement. Reproducible EQE-EL data were measured from MG-OLEDs using extended voltage sweeps (0–20 V), an example of a 1 cm^2 MG-OLED pixel is shown in Figure 5a. Current density (circles) and luminance (squares) curves demonstrated good measurement reproducibility. In contrast, ITO-OLED pixels, in general, demonstrated poor measurement reproducibility, an example of which is shown in Figure S5b, Supporting Information. Poor measurement reproducibility was noted at a reduced voltage range (0–12 V) for the ITO-OLED pixels. The differences in peak EQE between subsequent measurements were higher for ITO-OLEDs compared to MG-OLEDs (Figure 5b), which was maximum for the largest pixels (Pixel number 1 = 1 cm^2).

This trend for poor measurement reproducibility can be attributed to the heat generated during the measurements,

which can enhance EQE at lower temperatures, reversing quickly at a certain threshold.^[30] As the same metal grid layout is used for both sample sets and the EQE-EL spectra were measured in an integrating sphere, the light outcoupling efficiency was roughly constant, and any variation in the device EQE must, therefore, be dominated by the IQE changing during the experiment, indicating material changes occurring in the emissive layer. In the absence of an external heat sink, the measurement of relevant parameters for thick OLED pixels can be altered by the heat generated in the pixel during measurement. The reduced heat dissipation in the TCE from the lower effective sheet resistance in MG-OLEDs consequently affects other relevant OLED parameters in this thickness regime. As Joule heating from the TCE/active layer interface is reduced, less heat is transferred to the OLED, and thus the overall device stability will be improved.^[33] This indicates that the lowering of R_{sheet} using hybrid TCEs can provide a more robust and stable device fabrication platform for the investigation of temperature-sensitive light-emitting materials, as effects from Joule heating can be reduced during measurements. This is therefore beneficial to reproducibly measure the performance of OLED materials and may be of particular use for the investigation of thick, large-area devices.

The tendency for thick pixels to demonstrate irreproducible behavior during measurements can be further evidenced in the spectral shift seen in the normalized EL spectra of overheated ITO-OLED pixels (Figure S5b, Supporting Information) where the peak emission shifts from ≈ 553 to ≈ 540 nm. It should be noted that this effect was only observed in extreme cases in which pixels ceased emission following measurement (red curve). The peak EL emission wavelength was similar for MG- (black curve) and ITO- (blue curve) OLEDs (≈ 553 nm), consistent with previous reports on the color (and morphological) stability of SY comparing SY-OLEDs at annealing temperatures up to 200°C , after which the polymer morphology rapidly starts to degrade at 350°C .^[30] The slight change in the shoulder of the peak towards longer wavelengths could be related to the elevated temperature of the emissive layer at temperatures above the glass transition T_g causing aggregation of the polymer chains,^[34] and changes in the emission spectra of MEH-PPV polymers. This suggests that the operating temperatures in

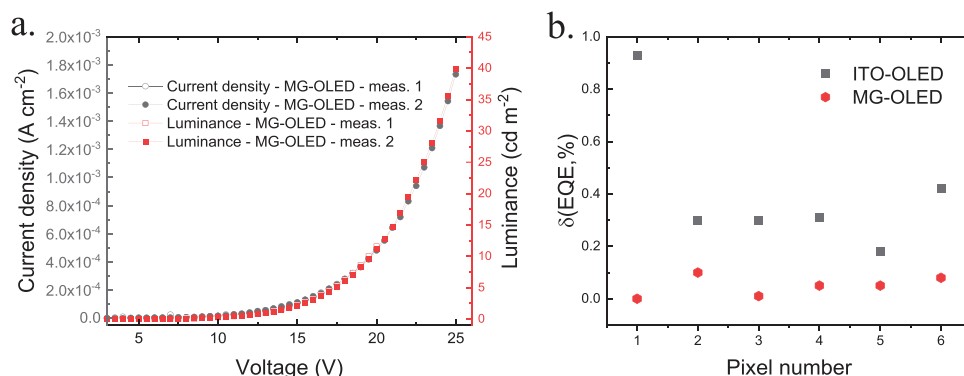


Figure 5. Comparison of 260 nm thick Super Yellow OLEDs. a.) Luminance (red squares, right axis) and current density (black circles, left axis) plotted against applied voltage for initial (unfilled) and subsequent (filled) measurements. For a 1 cm^2 metal grid (MG)–OLED pixel repeatedly measured between 0–20 V. b.) Difference in peak EQE between subsequent measurements on the same pixel for ITO-OLEDs (black squares) and MG-OLEDs (red hexagons). Pixel 1 device area = 1 cm^2 , other pixel device areas = 0.15 cm^2 .

parts of the ITO-OLEDs can exceed 200 °C, consistent with the trend of the heat generation results in this work. Previous reports have confirmed that the annealing temperature-dependent emission spectra of MEH-PPV and its derivatives are correlated with the formation of interchain species in the films, which will influence the aggregation and degradation behavior of related polymer types.^[34] Subsequent studies of MEH-PPV using variable angle spectroscopic ellipsometry (VASE) report aggregation behavior at annealing temperatures of 225 °C.^[35] For reference, the structures of MEH-PPV and Super Yellow are shown in Figure S6 a and b, Supporting Information, respectively. More generally, the operational lifetimes of other OLED types have been shown to be affected by temperature-dependent interlayer diffusion processes by neutron reflectometry.^[36] Even small amounts of interlayer mixing from annealing temperatures above 80 °C have been shown to quench the luminescence of the constituent layers.

Optimization of annealing conditions of the thicker pixels can be more accurately controlled during the device fabrication process and reproducibly measured on MG-OLEDs. Further, the temperature distribution across the active layer in the pixel will be more uniform during annealing using tailored device fabrication techniques (for example on a hot plate), compared to the increase in temperature during device operation, which is highest at the current injection areas for an ITO-OLED due to the profile of heat distribution at the TCE (Figure S3b, Supporting Information). For OLED investigations, the control of heat produced during the measurement process is an important consideration for material and device processing developments. This may be of particular significance for the investigation of tandem devices with multiple stacked emissive layers, such as the structures used to create white OLEDs (WOLEDs), which may also require high driving voltages.^[37] Multilayer device structures have been suggested as a method of producing high brightness OLED panels with long operational lifetimes.^[38] These types of thick junction OLED architectures will require TCEs with low sheet resistances to realize large-area OLEDs for lighting applications. Optimization of the design of metal grid structures requires consideration of the shading of the light-emitting regions, which is predicted by the geometrical fill factor of the grid structure. For large-area lighting applications, a fine mesh (narrow grid width and pitch) is preferable to reduce the visibility of the grid lines. The shadowing effect will cause local variations in the emitted light from the pixel, but cross-pixel uniformity will be improved due to the electrical properties of the MG-OLED.

The edges of the pixel being a likely point of failure due to increased flux current density could also have implications in the development of related solution-processed light-emitting devices, such as lasers. Impediments towards electrically pumped polymer injection lasers include high thresholds for lasing in currently investigated architectures, optical loss mechanisms, and high carrier injection/current densities.^[39,40] Light-emitting field-effect transistor (LEFET) architectures have been proposed to achieve electrically pumped lasing from Super Yellow on ITO/glass substrates, but it was estimated that current densities in the region of 60 kA cm⁻² may be required.^[41] At high current densities, the heat generated at the TCE will become even more significant. For device architectures that

require a transparent electrode and high current densities, the incorporation of metal grids may be a practical means of producing proof-of-concept devices.

3. Conclusions

In summary, finite element models of Super Yellow OLEDs on unmodified ITO (ITO-OLEDs) were compared to those on ITO with added metal grids (MG-OLEDs). Metal grids on the TCE reduce the potential drop across the surface, reducing the associated flux current through the TCE, and thereby lowering the Joule heating at the transparent electrode. The lower effective sheet resistance of the TCE in MG-OLEDs also produces higher current densities through the emissive layer.

A drift-diffusion model was used to generate current density-voltage profiles as a function of emissive layer thickness for a typical fluorescent material. Heat generation models were used on ITO- and MG-OLEDs to obtain estimates of their operational temperatures at different active layer thicknesses at comparable device currents. At 130 nm, the temperature in the TCE for a MG-OLED was estimated to be slightly cooler (≈ 310 K) compared to the equivalent ITO-OLED (≈ 360 K). At 260 nm, the difference in temperature of a MG-OLED (≈ 320 K) was more pronounced than the equivalent ITO-OLED (≈ 430 K).

Real Super Yellow ITO/MG -OLEDs were fabricated in two comparable thickness regimes. Thinner MG-OLED pixels (≈ 130 nm) demonstrated significant improvements in luminous flux and power efficiency. At this thickness, the measurements were reproducible, and the performance improvement consistent with a reduced sheet resistance at the TCE. In the thicker regime, MG-OLED pixels (≈ 260 nm) demonstrated improved measurement reproducibility and reliability compared to ITO-OLED pixels, attributed to the reduced Joule heating in the TCE. As the active layer thickness is increased, Joule heating from the TCE can cause material changes in the emissive layer, complicating the analysis of OLED devices. The addition of metal grids thus offers a facile method of improving OLED device performance and stability at larger active layer thicknesses and is particularly useful for solution-processed light-emitting devices with thick emissive layers and/or high current densities due to reduced heating effects at the TCE. The methods presented in this work are suited to the fabrication of prototype large-area OLED devices. Future innovations to reduce the processing costs of metal grids on TCEs will enable their use in large-area OLED panels for lighting applications.

4. Experimental Section

OLED Electrical Simulations: ITO- and MG-OLEDs were simulated using the commercially available large area organic solar simulator (LAOSS, Fluxim AG) software.^[42] The pixel sizes were 1 cm \times 1 cm and the TCE defined as a 100 nm thick layer of ITO in ITO-OLEDs, with additional hexagonal silver grid structures added on top of the ITO layer in MG-OLEDs. Unless otherwise stated, the thickness of the grid structures was 1 μ m, the radius was 1 mm, and the track width was 40 μ m. OLED devices were modeled as a 2D+1D+2D system, with a TCE, emissive layer, and metallic electrode. Values for the sheet resistances of ITO = 10 Ω \square^{-1} , Ag grid regions = 0.0159 Ω \square^{-1} , and Ag electrode = 0.159 Ω \square^{-1} . A small-area current density-voltage (JV) curve was used to define the electrical coupling (Figure 3a, emissive layer thickness = 130 nm).

Meshing conditions were set so that all simulations had as close to an equal number of finite elements to ensure similar precision across all simulations of ITO- and MG-OLEDs. Boundary conditions were set to reflect a realistic busbar setup: i) voltage was applied on two opposite edges of the top electrode, with the current tending to 0 on the remaining edges. ii) the bottom electrode was grounded on two opposing edges. These were kept constant in all simulations in this work. In electrical simulations, the voltages were varied between 0 and 25 V in steps of 0.5 V. The solving parameters were set for high performance and high memory requirements, using a nonlinear Newton solver with convergence parameters of absolute residual convergence type, root-mean-square normal, a tolerance of 1×10^{-7} , and a maximum iteration count of 100.

Small-Area JV Generation: The effect of varying the emissive layer thickness on the JV characteristics were modeled as using a 1D device model based on drift-diffusion.^[25] This model solves the continuity equations for electrons and holes within the emissive layer, taking into account the space charge effects via the Poisson equation. To ensure space-charge-limited current conduction, ohmic contacts with negligible contact resistance at the emissive layer-electrode interfaces were used. For the emissive layer, assumed to be trap-free and of thickness d , an electron mobility of $5 \times 10^{-6} \text{ cm}^2 \text{ Vs}^{-1}$, a hole mobility of $5 \times 10^{-5} \text{ cm}^2 \text{ Vs}^{-1}$, and a relative permittivity of 3 were used. Furthermore, a bandgap $E_g = 2.1 \text{ eV}$ and an effective density of states of $2.5 \times 10^{-19} \text{ cm}^{-3}$ for charge carriers were assumed. The recombination between electrons and holes in the emissive layer was assumed to be bimolecular Langevin recombination with the recombination coefficient given by $\frac{q(\mu_n + \mu_p)}{\epsilon \epsilon_0}$, where q is the elementary charge. At voltages $V > E_g/q$, the corresponding current density is well approximated by Equation (4) with $\zeta = 1.16$ and an effective built-in voltage $V_{bi} = 1.3 \text{ V}$.

OLED Electrothermal Simulations: The heat generation model available in LAOSS was used to investigate the effects of Joule heating from the TCE on OLED operating temperature with simulated JV characteristics described in the previous section. Unless otherwise stated, the simulation conditions were kept consistent with the electrical simulation section. Key input parameters for the OLED simulation were as follows: vertical thermal conductivity = $1.5 \text{ W m}^{-1} \text{ K}^{-1}$, ambient temperature = 300 K, heat transfer through ITO = $11 \text{ W m}^{-2} \text{ K}^{-1}$, heat transfer through Ag = $11 \text{ W m}^{-2} \text{ K}^{-1}$, and the OLED efficiency = 2.2%. The ambient temperature and OLED efficiency remained constant during the simulations in this work. Thermal sheet resistance of ITO = $1.37 \times 10^6 \text{ K W}^{-1} \square^{-1}$; thermal sheet resistance of the Ag electrode = $2.33 \times 10^4 \text{ K W}^{-1} \square^{-1}$. Additionally, key input parameters for the metal grid in the OLED simulation were as follows: vertical thermal conductivity = $430 \text{ W m}^{-1} \text{ K}^{-1}$, heat transfer through the anode = $3150 \text{ W m}^{-2} \text{ K}^{-1}$, and heat transfer through the cathode = $3150 \text{ W m}^{-2} \text{ K}^{-1}$. Due to the assumption of symmetric geometries of the electrodes used in the current solver, the Ag electrode was also assumed to have Ag grid "regions" in MG-OLEDs. These are assigned an electrical sheet resistance of $0.0159 \Omega \square^{-1}$ and a thermal sheet resistance of $2330 \text{ K W}^{-1} \square^{-1}$. Electrothermal simulations varied voltages between 0 and 8 V in steps of 0.25 V.

Metal Grid Fabrication: Photomasks for metal grid structures were designed in AutoCAD (width = 20 μm , pitch = 1 mm) to be compatible with commercially available 25 mm \times 25 mm patterned ITO/glass substrates (Kintec) and provide two separate ITO/metal grid regions on each substrate for the arrangement of the top electrodes. Hexagon structures were defined by their grid width and pitch (described in Figure S7a, Supporting Information), similar to the simulated TCE structures. The average visible transmission of grid structures was estimated using grid structures created on glass (with no ITO) with varying grid geometries (described in Figure S7ii, Supporting Information), confirming that the optical transmission of the grid structures varies linearly with the fraction shadowed. Substrates were cleaned using detergent (Alconox), deionized water, acetone, and isopropyl alcohol before lithographic processing.

Patterning of the grid features was implemented using a typical photolithography process using AZ ECI 3012 photoresist (spin-coated at 3000 rpm and soft baked at 100 $^\circ\text{C}$ for 1 min) The pattern

was exposed using an MA-8 mask aligner (Suss MicroTec) with an exposure dose of 110 mJ cm^{-2} at the i-line. The exposed features were developed in AZ 726 developer solution. The patterned substrates were cleaned in an O_2 plasma using an Oxford PlasmaLab 80 RIE system for 5 min. All photolithography related chemicals were purchased from MicroChemicals GmbH.

Stacks of 1 μm nickel/silver/aluminum were sputtered using a Kurt J. Lesker PVD 75 system. N-Methyl-2-pyrrolidone (NMP) at 50 $^\circ\text{C}$ was used to lift-off the metal structures, followed by brief ultrasonic agitation to remove residual metal particles. After microfabrication, substrates were cleaned using the process described above before optoelectronic device processing steps. The effective sheet resistance of the metal grid on ITO structures was $<1 \Omega \square^{-1}$, using a non-four-point uniform van der Pauw measurement on a parametric semiconductor analyzer (Keysight B1500A).

OLED Fabrication: Metal/ITO substrates were cleaned again following the above procedure following microfabrication and treated in ozone (Ossila UV/Ozone Cleaner) for 5 min. Two sample sets were prepared to investigate and compare MG- and ITO-OLEDs. Thinner SY OLED devices were fabricated as per the following procedure. PEDOT:PSS (Clevios, AI 4083) was syringe filtered onto the substrates (plain ITO and hybrid metal/ITO) and spin-coated at 6000 rpm before curing at 155 $^\circ\text{C}$ for 15 min to form the 30 nm thick hole transport layer. The commercially available light-emitting PPV copolymer, PDY-132, "Super Yellow" layers (8.5 mg mL^{-1} in toluene, both purchased from Sigma Aldrich) were spin-coated at 8500 rpm and baked at 55 $^\circ\text{C}$ for 5 min in a nitrogen glovebox, giving a film thickness of 130 nm. The SY thickness was confirmed using spectroscopic ellipsometry (J.A Woollam M-2000) on reference silicon pieces. Calcium/ silver (20/80 nm) electrodes were evaporated through a shadow mask using a glovebox-integrated Kurt J. Lesker Nano 36 system. Side profiles of the ITO-OLEDs, MG-OLEDs, and a top-down schematic of the MG-OLEDs are shown in Figure S7b, c, and d, Supporting Information, respectively. Thicker SY OLEDs were prepared as above, except molybdenum oxide (7 nm) was evaporated as the HTL layer. The above SY solution was spin-coated at 3000 rpm and baked at 55 $^\circ\text{C}$ for 5 min in a nitrogen glovebox, giving a reference film thickness of 260 nm. Top electrodes were evaporated as above. A portion of the samples was encapsulated using Cytop (AGC Chemicals), a spin-on dielectric material. 20% CYTOP (dissolved in CT-SOLV180, AGC) was spin-coated at 1000 rpm and baked at 55 $^\circ\text{C}$ for 5 min ($\approx 60 \text{ nm}$ thickness on reference films). A portion of the MG-OLED devices demonstrated short circuit behavior. This was attributed to the difficulty in conformally coating grid structures that are substantially thicker than the SY layer. Roughness in the metal grid regions from processing tended to exacerbate the likelihood of short circuits.

OLED Characterization: Super Yellow OLED devices were characterized using a calibrated EQE-EL measurement system (Hamamatsu C9920-12) comprising of a source measure unit (Keithley 2400), photonic multichannel analyzer, an integrating sphere, and a sample holder compatible with the fabricated devices. All aspects of the measurements were controlled using the supplied software. A photograph of an illuminated 1 cm^2 ITO-OLED pixel is shown in Figure S6e, Supporting Information.

Supporting Information

Supporting Information is available from the Wiley Online Library or from the author.

Acknowledgements

The work was supported by the Welsh Government Sêr Cymru Program through the European Regional Development Fund, Welsh European Funding Office and Swansea University strategic initiative in Sustainable Advanced Materials. A. A. received support from a Sêr Cymru II Rising Star Fellowship and P. M. is a Sêr Cymru II National Research Chair.

Conflict of Interest

The authors declare no conflict of interest.

Keywords

metallic grids, organic light-emitting diodes, transparent conductive electrodes

Received: July 17, 2020

Revised: September 21, 2020

Published online: November 9, 2020

-
- [1] B. Geffroy, P. le Roy, C. Prat, *Polym. Int.* **2006**, *55*, 572.
- [2] Z. Y. Xie, L. S. Hung, *Appl. Phys. Lett.* **2004**, *84*, 1207.
- [3] S. D. Yambem, M. Ullah, K. Tandy, P. L. Burn, E. B. Namdas, *Laser Photonics Rev.* **2014**, *8*, 165.
- [4] C. Sekine, Y. Tsubata, T. Yamada, M. Kitano, S. Doi, *Sci. Technol. Adv. Mater.* **2014**, *15*, 034203.
- [5] F. Templier, *OLED Microdisplays: Technology and Applications*, Wiley, Hoboken **2014**.
- [6] H. Sasabe, J. Kido, *J. Mater. Chem. C* **2013**, *1*, 1699.
- [7] A. Buckley, *Organic Light-Emitting Diodes (OLEDs): Materials, Devices and Applications*, Elsevier, Amsterdam **2013**.
- [8] P. Meredith, A. Armin, *Nat. Commun.* **2018**, *9*, 5261.
- [9] M. Morales-Masis, S. De Wolf, R. Woods-Robinson, J. W. Ager, C. Ballif, *Adv. Electron. Mater.* **2017**, *3*, 1600529.
- [10] W. Cao, J. Li, H. Chen, J. Xue, *J. Photonics Energy* **2014**, *4*, 040990.
- [11] M. Reinhard, R. Eckstein, A. Slobodskyy, U. Lemmer, A. Colmann, *Org. Electron.* **2013**, *14*, 273.
- [12] M. Zhang, S. Höfle, J. Czolk, A. Mertens, A. Colmann, *Nanoscale* **2015**, *7*, 20009.
- [13] A. J. Stapleton, R. A. Afre, A. V. Ellis, *Sci. Technol. Adv. Mater.* **2015**, *16*, 025002.
- [14] S. D. Yambem, A. Halder, K. S. Liao, E. P. Dillon, A. R. Barron, S. A. Curran, *Sol. Energy Mater. Sol. Cells* **2011**, *95*, 2424.
- [15] L. Zhou, M. Yu, X. Chen, S. Nie, W.-Y. Lai, W. Su, Z. Cui, W. Huang, *Adv. Funct. Mater.* **2018**, *28*, 1705955.
- [16] D. Li, W. Y. Lai, Y. Z. Zhang, W. Huang, *Adv. Mater.* **2018**, *30*, 1704738.
- [17] W. J. Hyun, E. B. Secor, M. C. Hersam, C. D. Frisbie, L. F. Francis, *Adv. Mater.* **2015**, *27*, 109.
- [18] A. Shimoni, S. Azoubel, S. Magdassi, *Nanoscale* **2014**, *6*, 11084.
- [19] T. Cheng, Y. Z. Zhang, J. P. Yi, L. Yang, J. D. Zhang, W. Y. Lai, W. Huang, *J. Mater. Chem. A* **2016**, *4*, 13754.
- [20] R. E. Triambulo, J. W. Park, *Org. Electron.* **2016**, *28*, 123.
- [21] K. J. Bergemann, R. Krasny, S. R. Forrest, *Org. Electron.* **2012**, *13*, 1565.
- [22] A. Kirch, A. Fischer, M. Liero, J. Fuhrmann, A. Glitzky, S. Reineke, *Light: Sci. Appl.* **2020**, *9*, 5.
- [23] J. Park, J. Lee, Y. Y. Noh, *Org. Electron.* **2012**, *13*, 184.
- [24] A. Luque, S. Hegedus, *Handbook of Photovoltaic Science and Engineering*, Wiley, Chichester, UK, **2011**.
- [25] O. J. Sandberg, M. Nyman, R. Österbacka, *Phys. Rev. Appl.* **2014**, *1*, 024003.
- [26] M. Lampert, *Current Injection in Solids*, Academic Press, New York, **1970**.
- [27] R. H. Parmenter, W. Ruppel, *J. Appl. Phys.* **1959**, *30*, 1548.
- [28] G.-J. A. H. Wetzelaer, N. J. Van der Kaap, L. J. A. Koster, P. W. M. Blom, *Adv. Energy Mater.* **2013**, *3*, 1130.
- [29] O. J. Sandberg, A. Armin, *Synth. Met.* **2019**, *254*, 114.
- [30] S. Burns, J. MacLeod, T. Trang Do, P. Sonar, S. D. Yambem, *Sci. Rep.* **2017**, *7*, 40805.
- [31] V. C. Bender, N. D. Barth, F. B. Mendes, R. A. Pinto, T. B. Marchesan, J. M. Alonso, in *IEEE Int. Symp. Ind. Electron.*, IEEE, Buzios **2015**, pp. 1190–1195.
- [32] Y. Kim, C.-S. Ha, *Advances in Organic Light-Emitting Devices*, Trans Tech Publications, Aedermannsdorf, Switzerland **2008**, pp. 87–97.
- [33] P. E. Burrows, Z. Shen, V. Bulovic, D. M. McCarty, S. R. Forrest, J. A. Cronin, M. E. Thompson, *J. Appl. Phys.* **1996**, *79*, 7991.
- [34] J. Liu, T. F. Guo, Y. Yang, *J. Appl. Phys.* **2002**, *91*, 1595.
- [35] O. P. M. Gaudin, I. D. W. Samuel, S. Amriou, P. L. Burn, *J. Appl. Phys.* **2020**, *127*, 093101.
- [36] P. L. Burn, J. A. McEwan, A. J. Clulow, R. Wang, A. Nelson, I. R. Gentle, *SID Int. Symp. Dig. Tech. Pap.* **2017**, *48*, 1129.
- [37] J. W. Park, D. C. Shin, S. H. Park, *Semicond.: Sci. Technol.* **2011**, *26*, 034002.
- [38] J. Spindler, M. Kondakova, M. Boroson, J. Hamer, V. Gohri, M. Büchel, M. Ruske, E. Meulancamp, *SID Int. Symp. Dig. Tech. Pap.* **2016**, *47*, 294.
- [39] M. Reufer, S. Riechel, J. M. Lupton, J. Feldmann, U. Lemmer, D. Schneider, T. Benstem, T. Dobbertin, W. Kowalsky, A. Gombert, K. Forberich, V. Wittwer, U. Scherf, *Appl. Phys. Lett.* **2004**, *84*, 3262.
- [40] P. Görrn, T. Rabe, T. Riedl, W. Kowalsky, *Appl. Phys. Lett.* **2007**, *91*, 041113.
- [41] E. B. Namdas, M. Tong, P. Ledochowitsch, S. R. Mednick, J. D. Yuen, D. Moses, A. J. Heeger, *Adv. Mater.* **2009**, *21*, 799.
- [42] C. Kirsch, S. Altazin, R. Hiestand, T. Beierlein, R. Ferrini, T. Offermans, L. Penninck, B. Ruhstaller, *Int. J. Multiphys.* **2017**, *11*, 127.